JOURNAL OF SPACECRAFT AND ROCKETS
Vol. 43, No. 2, March–April 2006

Transition Due to Heat-Shield Cavities on a Mars Entry Vehicle

Brian R. Hollis* and Derek S. Liechty†
NASA Langley Research Center, Hampton, Virginia 23681

The influence of heat-shield cavities on the forebody of the proposed Mars Science Laboratory entry vehicle has been investigated experimentally and computationally. Wind-tunnel tests were conducted on the 70-deg sphere-cone forebody of the vehicle with various cavity sizes and locations to assess their effects on convective heating and boundary-layer transition. The heat-transfer coefficients and transition locations were measured using global phos-phor thermography. Laminar and turbulent Navier–Stokes computations were performed to compare with the experimental aeroheating data and to determine boundary-layer parameters for use in correlation of the experimental transition data. Comparisons of laminar heating data and computations were found to agree to within the experimental uncertainty, but turbulent computations underpredicted measured heating levels by up to 20%, possibly because the cavities were not included in the simple computational geometry employed. The cavity transition data were analyzed to determine a correlation for transition to turbulence at a cavity in terms of cavity geometric parameters and computed boundary-layer conditions. This correlation was used to show that the vehicle could experience early onset of turbulent flow in flight as a result of the presence of cavities.

Nomenclature

a_w	=	speed of sound at wall, m/s
H_{AW}	=	adiabatic enthalpy, J/kg
H_w	=	wall enthalpy, J/kg
H_0	=	total enthalpy, J/kg
h	=	heat-transfer coefficient, kg/m^2/s, $q/(H_{\mathrm{AW}}-H_w)$
h_{FR}	=	Fay–Riddell heat-transfer coefficient, kg/m^2/s
M_e	=	boundary-layer edge Mach number
M_∞	=	freestream Mach number
p_∞	=	freestream pressure, N/m^2
q	=	heat-transfer rate, W/m^2
R	=	base (maximum) radius, m
R_c	=	corner radius, m
R_n	=	nose radius, m
Re_{cell}	=	wall cell Reynolds number, $(\rho_w a_w \Delta s)/\mu_w$
$(Re_{w,e})_{\mathrm{turb}}$	=	critical Reynolds number for turbulence, $(\rho_e U_e w)/\mu_e$
Re_θ	=	boundary-layer momentum thickness Reynolds number, $(\rho_e U_e \theta)/\mu_{\mathrm{we}}$
Re_∞	=	freestream unit Reynolds number, 1/m
r	=	radial position, m
T_∞	=	freestream temperature, K
U_∞	=	freestream velocity, m/s
w	=	cavity diameter, cm
α	=	angle of attack, deg
Δs	=	wall cell height, m
δ	=	boundary-layer thickness, m
θ	=	boundary-layer momentum thickness, m
μ_w	=	wall cell viscosity, kg/m/s
ρ_w	=	wall cell density, kg/m^3
ρ_∞	=	freestream density, kg/m^3
ϕ	=	model rotation, deg

Received 7 August 2002; revision received 1 August 2004; accepted for publication 1 February 2005.

*Aerospace Technologist, Aerothermodynamics Branch. Senior Member AIAA.

†Aerospace Technologist, Aerothermodynamics Branch.

Introduction

THE Mars Science Laboratory (MSL) mission[1,2] is intended to perform a precision landing of a scientific payload on Mars and is currently scheduled for launch in 2009. Research presented herein is based on an earlier design for launch in 2007. One of the important design issues for this vehicle was the determination of whether the boundary layer on the forebody of the entry vehicle would be laminar or turbulent. This issue was more complicated than was the case for previous Mars missions, because the 2007 MSL forebody design did not have a smooth, unbroken surface; instead, there were six circular cavities in the forebody heat shield where bolts would be used to attach the vehicle to a cruise stage during transit from Earth.

The goal of the present study was to formulate transition criteria for the MSL, which accounted for cavity cavity parameters and flowfield conditions. To accomplish this goal, wind-tunnel tests were conducted to generate a transition database, and then Navier–Stokes computations were performed at the wind-tunnel conditions to determine boundary-layer edge quantities, which were used to correlate the transition data. The computations and correlations are presented in this paper, and the wind-tunnel tests are detailed in the companion paper by Liechty et al.[3] Comparisons of both laminar and turbulent aeroheating predictions with the experimental data are also presented herein. Additionally, a detailed investigation of the MSL aeroheating environment during Mars entry is presented in the companion paper by Edquist et al.[4] A similar study on cavity effects was performed by Cheatwood et al.[5] for the Genesis mission.

Mars Smart Lander Geometry

The proposed Mars Smart Lander entry vehicle 2007 design was a 70-deg half-angle sphere cone with a biconic afterbody (Fig. 1). The forebody had six circular cavities spaced at 60-deg increments through which bolts would attach it to a carrier vehicle during transit to Mars (Fig. 2). In this study, various cavity diameters and radial and angular positions were investigated to determine their effects on boundary-layer transition and surface aeroheating levels.

Computational Method

Computations were performed using the LAURA (Langley Aerothermodynamic Upwind Relaxation Algorithm) code,[6,7] a three-dimensional, finite volume solver, which includes perfect-gas, equilibrium, and nonequilibrium chemistry models. The code can be used to solve the inviscid, thin-layer Navier–Stokes, or full Navier–Stokes equations. For the current study, the thin-layer mode was employed; it was concluded in Ref. 5 from computations on a

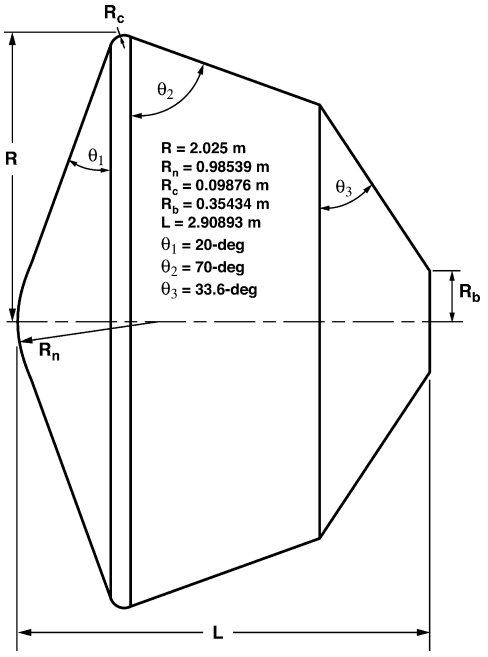

Fig. 1 Dimensions of full-scale Mars Science Laboratory entry vehicle (2007 design).

Fig. 2 Mars Science Laboratory entry vehicle and cruise stage (2007 design).

similar blunt body that this mode provided accurate results for attached forebody flows. Time integration to steady state in LAURA is accomplished through a point-relaxation scheme. Roe averaging[8] with Harten's entropy fix[9] and Yee's symmetric total-variation-diminishing limiter[10] is used for inviscid fluxes, and a second-order scheme is employed for viscous fluxes. For turbulent computations, the algebraic Baldwin–Lomax[11] model with modifications[12] for compressible flow and the Dhawan–Narashima[13] transition model were employed. In this study, the perfect-gas air model was used for the wind-tunnel computations, whereas for the flight cases discussed in Ref. 4 an eight-species, nonequilibrium, nonionizing Martian atmosphere model (CO_2, CO, N_2, O_2, NO, C, N, O) was used.

Freestream conditions for the wind-tunnel computations were set to the nominal freestream operating conditions of the NASA Langley Research Center (LaRC) 20-Inch Mach Air Tunnel, which are listed in Table 1, and a uniform, ambient 300 K wall temperature boundary condition was imposed. The use of a constant wall temperature was valid because the experimental data are reported in terms of the nondimensional ratio h/h_{FR}, which is assumed to remain constant with wall temperature. The quantity h_{FR} is the heat-transfer coefficient computed using the Fay–Riddell method[14] method with the same nose radius as the MSL model at a wall temperature of 300 K (540°R).

Table 1 Freestream conditions for wind-tunnel cases

Re_∞, 1/m	M_∞	T_∞, K	ρ_∞, kg/m^3	U_∞, m/s	h_{FR}, kg/m$^2\cdot$s	q_{FR}, W/cm^2
6.7×10^6	5.95	62.0	3.35×10^{-2}	938.6	0.283	5.70
8.5×10^6	5.97	62.2	4.05×10^{-2}	943.0	0.313	6.45
9.8×10^6	5.98	62.2	4.62×10^{-2}	944.4	0.335	6.95
1.1×10^7	5.99	61.6	5.29×10^{-2}	940.1	0.356	7.25
1.4×10^7	6.00	61.3	6.41×10^{-2}	940.4	0.392	7.95
1.7×10^7	6.02	63.4	7.92×10^{-2}	958.7	0.446	9.92
1.9×10^7	6.03	62.8	8.99×10^{-2}	955.6	0.474	10.4
2.4×10^7	6.06	62.3	1.13×10^{-1}	954.6	0.529	11.5

A structured, finite volume, multiple-block grid with a singularity-free nose was employed for the computations. The grid contained approximately 230,000 points with a body-normal resolution of 65 points. Grid adaptation was performed (as per the method detailed in Ref. 7) to align the grid with the bow shock and to produce nominal wall cell Reynolds numbers on the order of $Re_{\mathrm{cell}} = 10$ or less.

The effects of normal grid-point resolution on the computed heating distributions were examined by repeating the computations for the $\alpha = 16$ deg, $Re_\infty = 1.9\times10^7$/m case with grids containing half (32) and twice (128) as many cells in the normal direction as the nominal grid (64). The heating distributions from these computations are shown in Fig. 3. Heating levels dropped nearly uniformly over the entire surface by about 5% from the 32-cell grid to the 64-cell grid, but from the 64-cell grid to the 128-cell grid heating levels dropped by about 1% except around the stagnation region, where the decrease was approximately 2%. Therefore, it was concluded that the original 64 normal cell grid provided acceptable accuracy for this study.

Although the wind-tunnel test models were fabricated with cavities to replicate those in the flight vehicle heat shield, they were not included in the MSL computational geometry. Thus, the effects of the cavities on the flowfield were not modeled in the computations. Instead, the effects of the cavities on the state of the boundary layer were simulated by specifying that transition began at the cavity location. To attempt to bound the effects of the cavities on boundary-layer transition, the transition length in the Dhawan–Narashima transition model was specified as either zero, to simulate an immediate jump to fully developed turbulent flow, or as equal to the running length of the boundary layer from the nose of the vehicle to the cavity location to simulate natural transition.

Experimental Method

The wind-tunnel testing, which complements this computational study, is presented in detail in Ref. 3, and a brief discussion is included herein for completeness. The tests were conducted in the NASA LaRC 20-Inch Mach 6 Air Tunnel.[15,16] Representative flow conditions for each of the standard 20-Inch Mach 6 Air Tunnel operating points have been computed using the GASPROPS[17] code and are listed in Table 1.

Global surface heating distributions were obtained using the digital optical measurement method of two color, relative-intensity, phosphor thermography.[18–21] As discussed in Ref. 3, the estimated experimental uncertainty of the heating data in this study was approximately ±13%. The heating data are presented in the nondimensional form h/h_{FR}, where h_{FR} is the reference heat-transfer coefficient from Fay–Riddell theory for a 300 K (540°R) surface temperature and the nose radius of the model. In the definitions of both h and h_{FR}, the adiabatic wall enthalpy H_{aw} is assumed to be equal to the total enthalpy H_0.

Heating distributions were measured on 0.0314-scale ceramic models of the MSL entry vehicle. Model parametrics were cavity diameter ($w = 7.62$, 5.59, or 3.81 cm full scale); angular location of the cavity (with respect to the lee-side centerline); and radial location of the cavity ($r/R = 0.41$ or 0.70). These parametrics are shown in Fig. 4. Note that the actual flight vehicle would have six cavities of uniform diameter at a constant radial location separated by

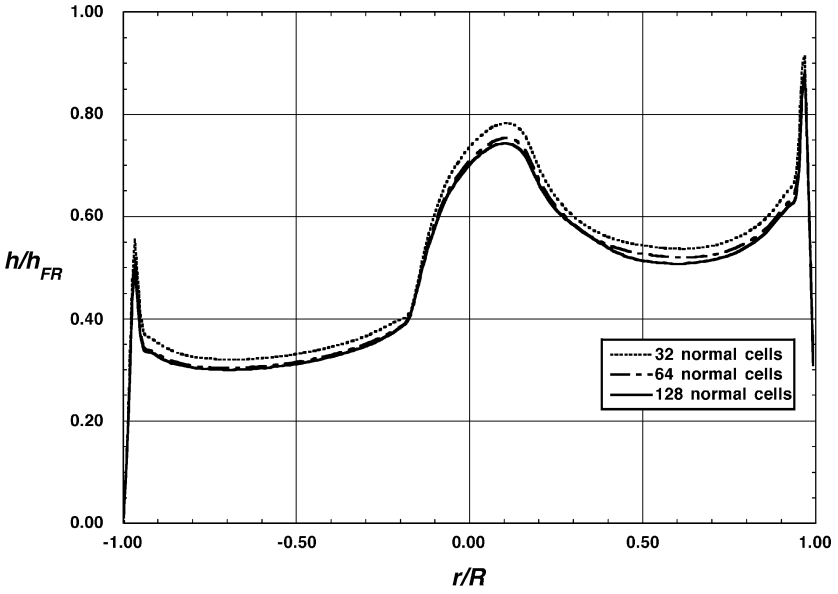

Fig. 3 Effects of normal grid resolution on computed heating levels: $\alpha = 16$ and $Re_\infty = 2.4 \times 10^7$/m.

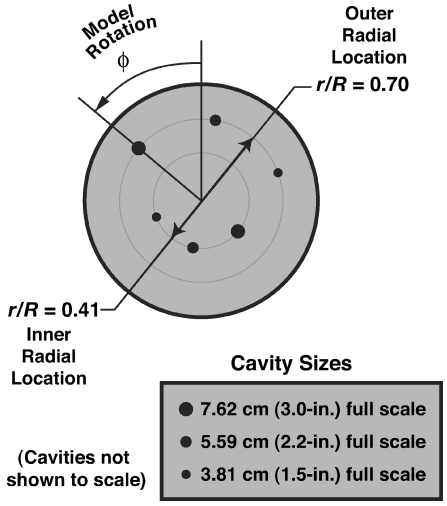

Fig. 4 Layout of cavities on MSL model.

60-deg rotational increments; the current arrangement was designed to maximize the number of parametrics, which could be studied during each run.

Aeroheating Predictions and Comparisons with Experimental Data

Laminar Comparisons

Laminar computations were performed at the conditions listed in Table 1 for angles of attack of 0, 11, 16, and 20 deg. Symmetry-plane comparisons of these computed heating distributions with the wind-tunnel data for each angle of attack are presented in Figs. 5–8. In these figures, the experimental data shown were measured on models without cavities. The computed laminar heating distributions were found to agree with the experimental data to within the estimated uncertainty of $\pm 13\%$ for all cases except at the forebody corners.

Turbulent Comparisons

Turbulent computations were performed for wind-tunnel conditions of $Re_\infty = 1.4 \times 10^7$/m to 2.4×10^7/m at $\alpha = 16$ deg, which was the nominal angle of attack at peak heating on the 2007 vehicle flight trajectory. Because boundary-layer transition in the experiment was produced by cavities in the test models (as it would also occur in flight) as opposed to naturally, transition in the computations was modeled in several different ways to attempt to reproduce the data. Computations were performed with the boundary layer fully turbulent over the length of the vehicle, with natural transition beginning at the location of the cavity, and with zero-length transition to fully turbulent flow at the cavity location. For the natural transition computations, the transition length was set equal to the running length of the flow from the nose to the cavity.

Symmetry-plane comparisons of these computations with the experimental data for both radial cavity locations are shown for $r/R = 0.41$, $Re_\infty = 1.4 \times 10^7$/m, 1.9×10^7/m, and 2.4×10^7/m in Figs. 9–11 and for the same Reynolds numbers with $r/R = 0.70$ in Figs. 12–14. In both sets of figures, comparisons are shown only for the lee side of the vehicle because the wind-side cavity was observed to have little or no effect on the heating except at the cavity itself for most cases. The agreement between measurement and prediction was a function of the transition length and location specified for the computations. The agreement was also a function of cavity size and freestream Reynolds number.

As shown in Figs. 9–14, both the location at which transition was specified to begin and the length of transition which was specified had significant effects on the computed heating levels. For both radial locations of transition onset, the heating levels computed by assuming fully turbulent flow beginning at the specified radial position (i.e., zero-length transition) were higher than those computed when the flow was treated as fully turbulent from the nose of the vehicle. This difference was because the boundary-layer thickness at a given location was greater for the fully turbulent flow from the nose because of the longer running length over which the turbulent boundary layer had to grow. Similarly, the boundary-layer thickness at a given location (downstream of the end of transition) was greater when zero-length transition was specified at the cavity location than when natural transition was specified. Hence, for the cavity location of $r/R = 0.40$ the heating levels at a given location with zero-length transition specified were lower than those at the same point with natural transition specified because the boundary layer was thicker. However, for the $r/R = 0.70$ cavity case the boundary layer was still transitional at the shoulder of the vehicle when natural transition was specified, so that comparison with the zero-transition length computation was not appropriate.

Inner-Cavity Location Comparisons

At the lowest Reynolds number of $Re_\infty = 1.4 \times 10^7$/m (Fig. 9), the smallest cavity had no effect on the heating, and the intermediate cavity had only a slight effect. These two data sets compared well with the laminar predictions. Although a more significant heating increase was produced by the largest cavity, the heating levels only

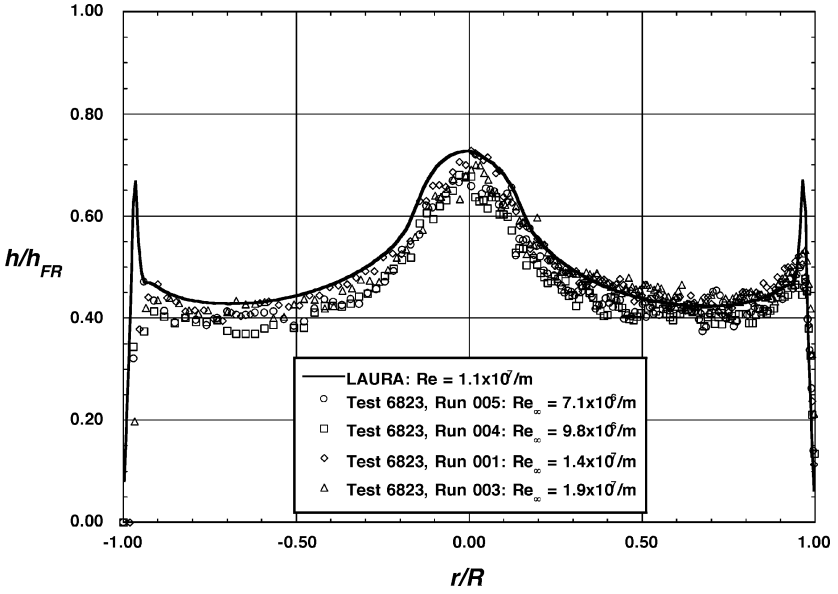

Fig. 5 Laminar centerline heating comparison for $\alpha = 0$ deg.

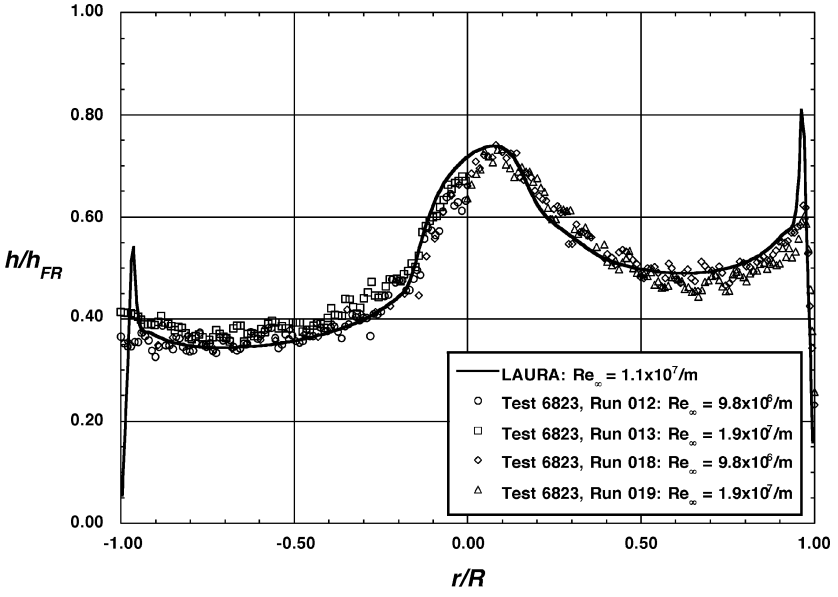

Fig. 6 Laminar centerline heating comparison for $\alpha = 11$ deg.

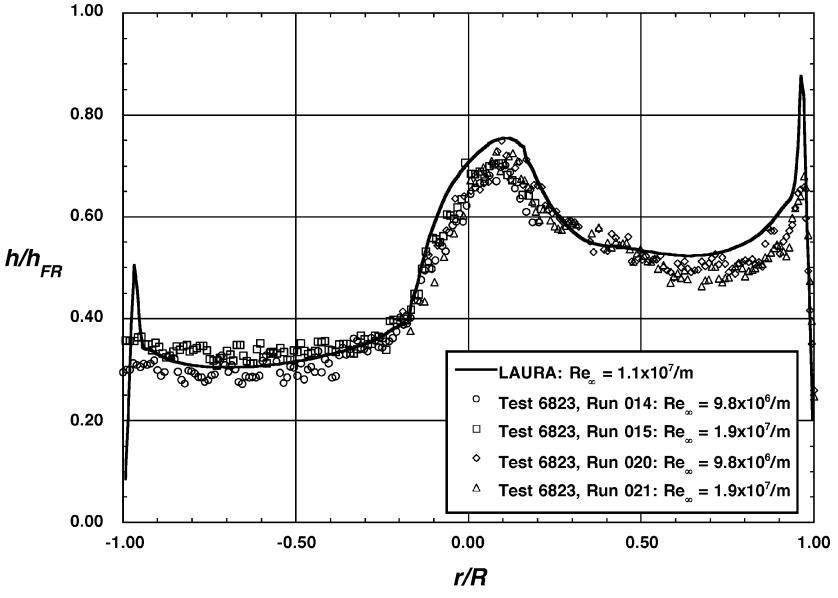

Fig. 7 Laminar centerline heating comparison for $\alpha = 16$ deg.

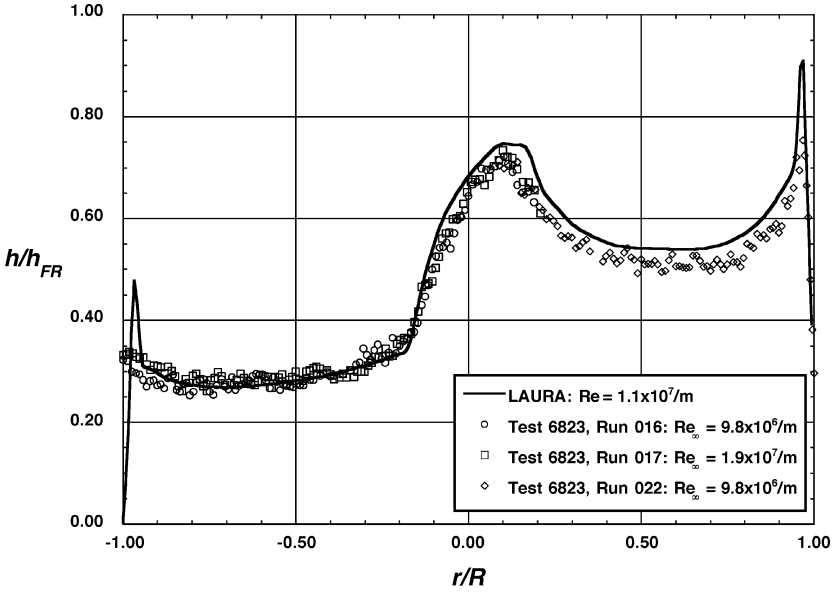

Fig. 8 Laminar centerline heating comparison for $\alpha = 20$ deg.

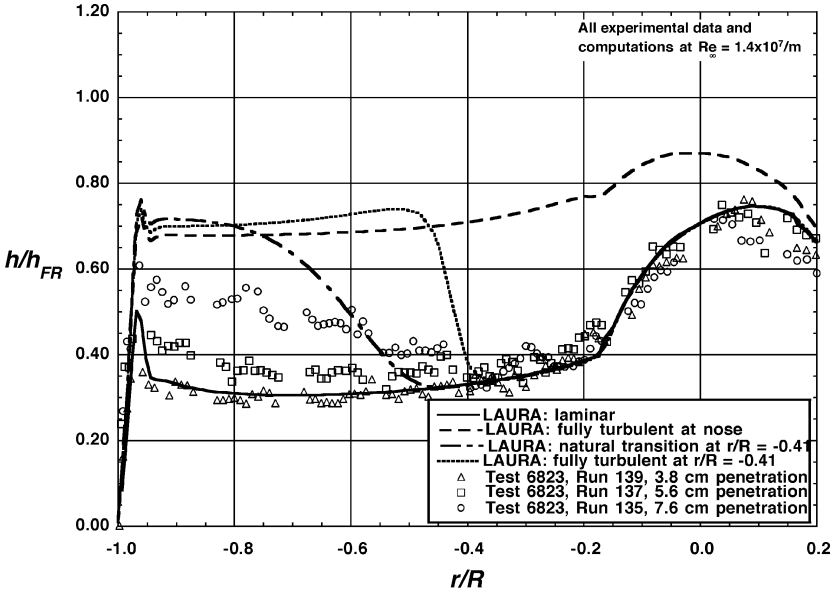

Fig. 9 Turbulent lee-side centerline comparison for $\alpha = 16$, $Re_\infty = 1.4 \times 10^7$/m, and $r/R = 0.41$.

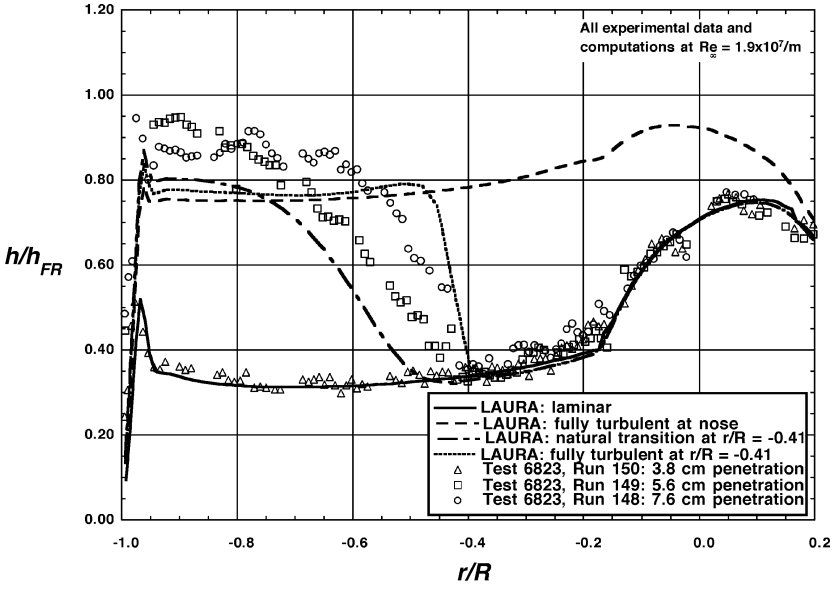

Fig. 10 Turbulent lee-side centerline comparison for $\alpha = 16$, $Re_\infty = 1.9 \times 10^7$/m, and $r/R = 0.41$.

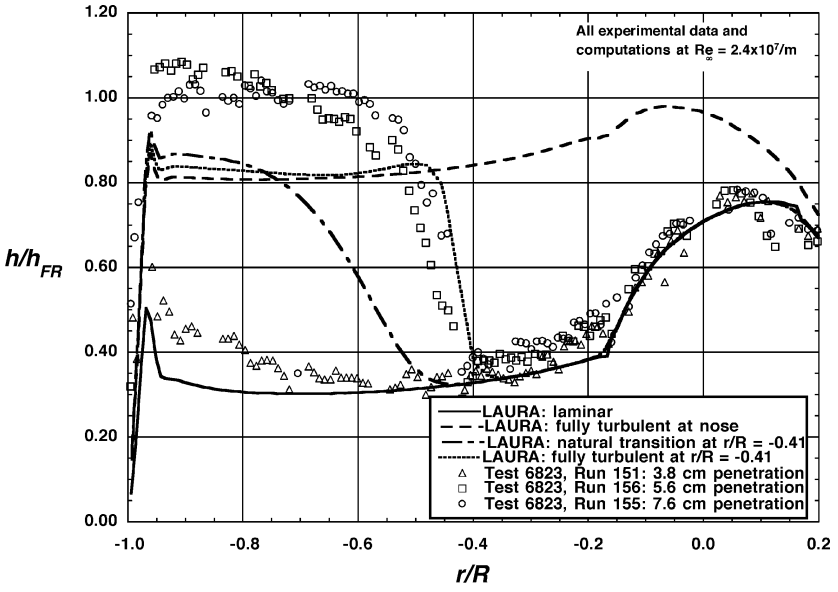

Fig. 11 Turbulent lee-side centerline comparison for $\alpha = 16$, $Re_\infty = 2.4 \times 10^7$/m, and $r/R = 0.41$.

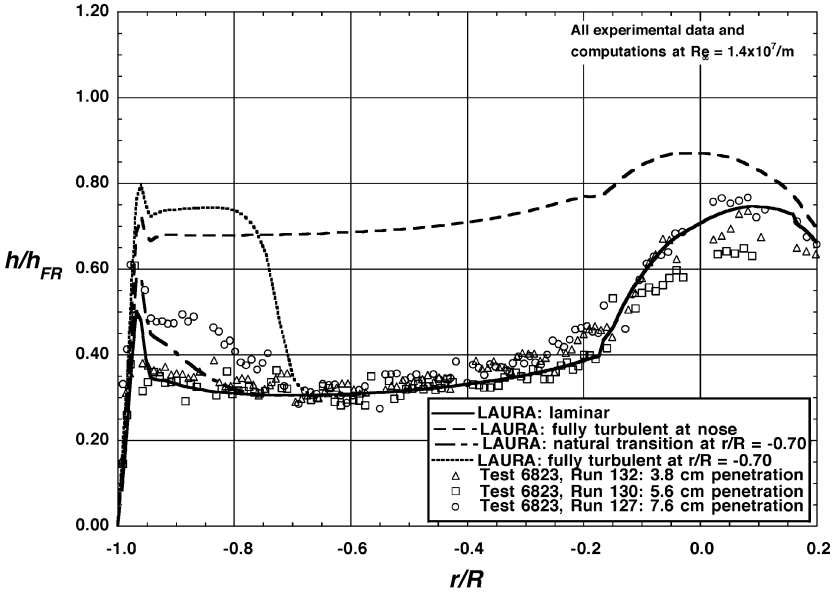

Fig. 12 Turbulent lee-side centerline comparison for $\alpha = 16$, $Re_\infty = 1.4 \times 10^7$/m, and $r/R = 0.70$.

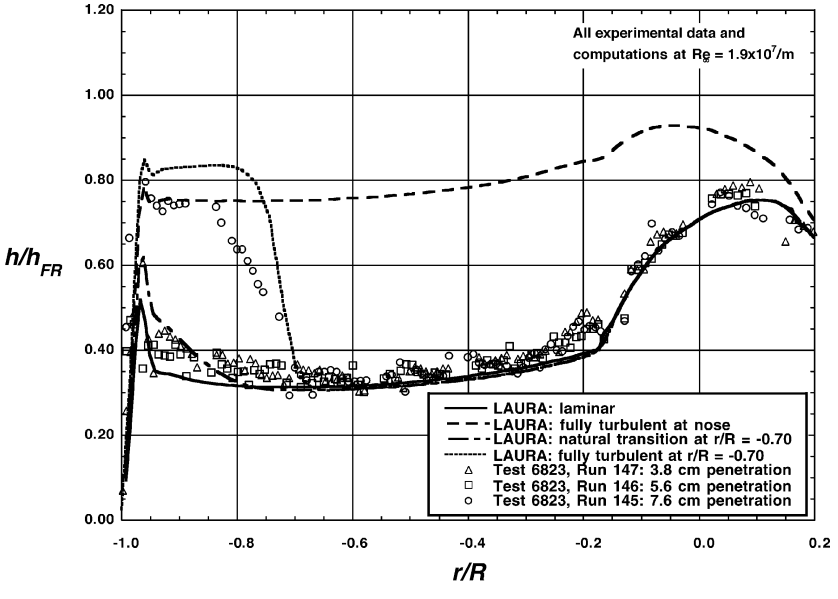

Fig. 13 Turbulent lee-side centerline comparison for $\alpha = 16$, $Re_\infty = 1.9 \times 10^7$/m, and $r/R = 0.70$.

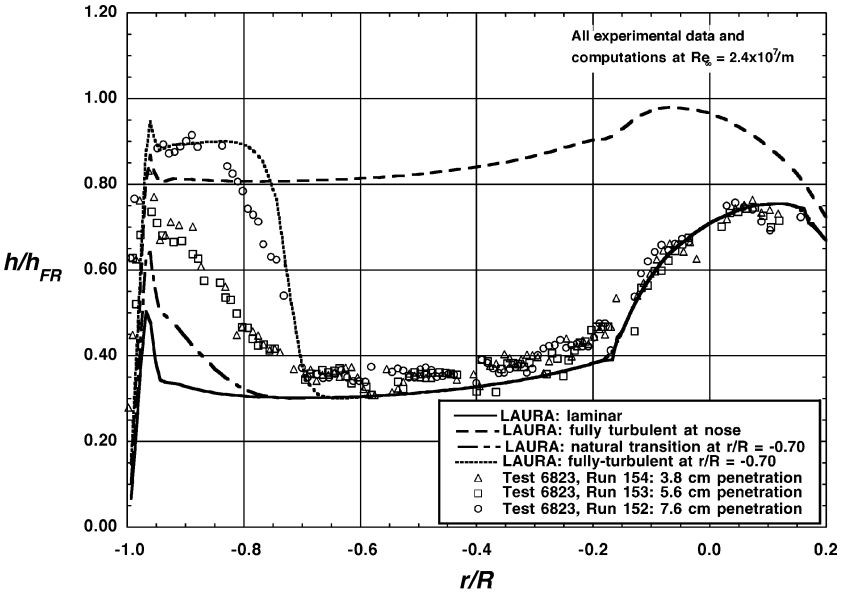

Fig. 14 Turbulent lee-side centerline comparison for $\alpha = 16$, $Re_\infty = 2.4 \times 10^7$/m, and $r/R = 0.70$.

rose gradually over the length of the vehicle and never reached a "plateau" typical of fully developed turbulent flow. For this case, the measured heating levels fell between the laminar and natural-transition predictions.

At the intermediate Reynolds number of $Re_\infty = 1.9 \times 10^7$/m (Fig. 10), the data for the smallest cavity appeared to remain laminar and matched the laminar computation. The heating distributions for the two larger cavities had shapes similar to the natural transition prediction, but the peak values were higher than either the natural or zero-length transition predictions by more than 15 to 20%, which was outside the range of experimental uncertainty.

At the highest Reynolds number, of $Re_\infty = 2.4 \times 10^7$/m (Fig. 11), the beginning of transition was noted downstream of the smallest cavity, but the boundary layer did not appear to develop into fully turbulent flow. The shapes of the heating distributions for the two larger cavities were similar to the zero-length transition predictions, but the peak heating levels were again 15–20% higher than the computed values. The data for this condition represent the worst case for cavity heating effects, with the cavity-induced turbulent heating levels exceeding the nose heating levels by 25%.

Outer-Cavity Location Comparisons

The outer cavity location ($r/R = 0.70$) cases were not as well suited for comparison with predictions as the inner ($r/R = 0.41$) cases because the boundary layer did not have sufficient running length downstream from the cavity for fully turbulent flow to develop. Significant heating augmentation was observed in the experimental data for the largest hole size at all Reynolds numbers and for the two smaller holes at the highest Reynolds number. At $Re_\infty = 1.4 \times 10^7$/m (Fig. 12), the heating data for the largest cavity fell between the natural and zero-length transition predictions. For the two higher Reynolds numbers (Figs. 13 and 14), the large cavity heating distributions appeared to match the shape of the zero-length transition prediction, but in terms of the heating levels the $Re_\infty = 1.9 \times 10^7$/m data were approximately 10 to 15% lower than the zero-length transition prediction, whereas the $Re_\infty = 2.4 \times 10^7$/m data closely matched the prediction.

Assessment of Cavity Data Comparisons

The present method for predicting turbulent heating levels, an algebraic turbulence model with a specified transition location and a transition length varied between zero and the running length ahead of the transition location, appeared to bound the experimental heating data for the range of Reynolds numbers and cavity sizes for the $r/R = 0.70$ cavity location. However, for the $r/R = 0.41$ cavity location the present method underpredicted the measured peak

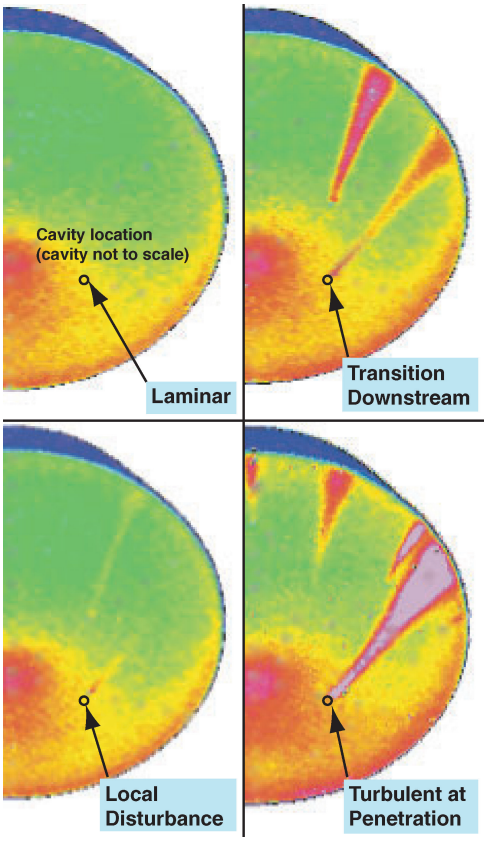

Fig. 15 Classification of cavity effect on boundary layer.

heating levels by up to 20%, although the shape of the heating distributions was approximately reproduced. The most likely reasons for these differences were that the heat-shield cavities were not included in the computational geometry, and thus their possible effects on the flowfield (e.g., circulation within the cavities, shocks at the lip of the cavities, boundary-layer separation, and vortex formation downstream of the cavities) were not predicted.

In a similar study[5] for the Genesis mission, the cavity was modeled in the computational geometry. It was found in that study that the presence of the cavity had significant effects both on heating around the cavity itself, where a localized spike in the heating levels was predicted, and downstream of the cavity, where turbulent

heating levels lower than without the cavity were predicted. However, it was also concluded in that study that the simple algebraic transition/turbulence models used (the same as used in this study) were not sufficient to resolve the effects of the cavity even with the cavity included in the computational geometry.

Implications for Heat-Shield Design

In terms of design criteria, the worst case for heating, based on the experimental data, would be a cavity at $r/R = 0.41$ of sufficient diameter to cause transition because the boundary layer has greater running length downstream of the cavity for turbulent flow to develop than it would have for a cavity at $r/R = 0.70$. This case with an $r/R = 0.41$ cavity, which produced transitional/turbulent flow, is represented by the data for the two larger cavities at $Re_\infty = 2.4 \times 10^7$/m (Fig. 11). For this case, the measured turbulent heating levels downstream of the cavity were approximately 25% higher than at the nose. In comparison to predicted values, these experimental heating levels were approximately 10% higher than the predicted fully turbulent levels at the nose and were approximately 20% higher than those predicted downstream of the cavity using the zero-length transition model.

Boundary-Layer Transition Data and Correlations

A database of approximately 800 boundary-layer-state data points, which covered the range of angles of attack, freestream Reynolds numbers, cavity diameters, and cavity radial locations, was generated during the wind-tunnel testing. For each data point, the state of the boundary layer downstream of the cavity was determined through visual inspection of the surface heating images and classified as either laminar, local disturbance at cavity, transition downstream of cavity, or fully turbulent at cavity. Examples of experimental data that fit each of these classifications are shown in Fig. 15. These classifications are somewhat simplified descriptions of a complex flowfield and should be used with care. For example, for a data point classified as "local disturbance," the heating levels measured near the cavity might be higher than heating levels downstream

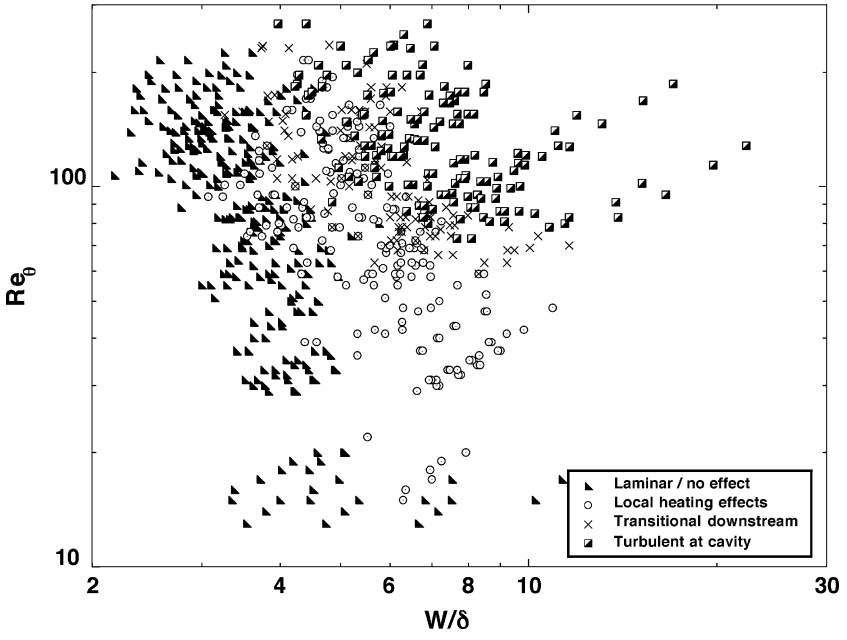

Fig. 16 Cavity effects as a function of Re_θ and w/δ.

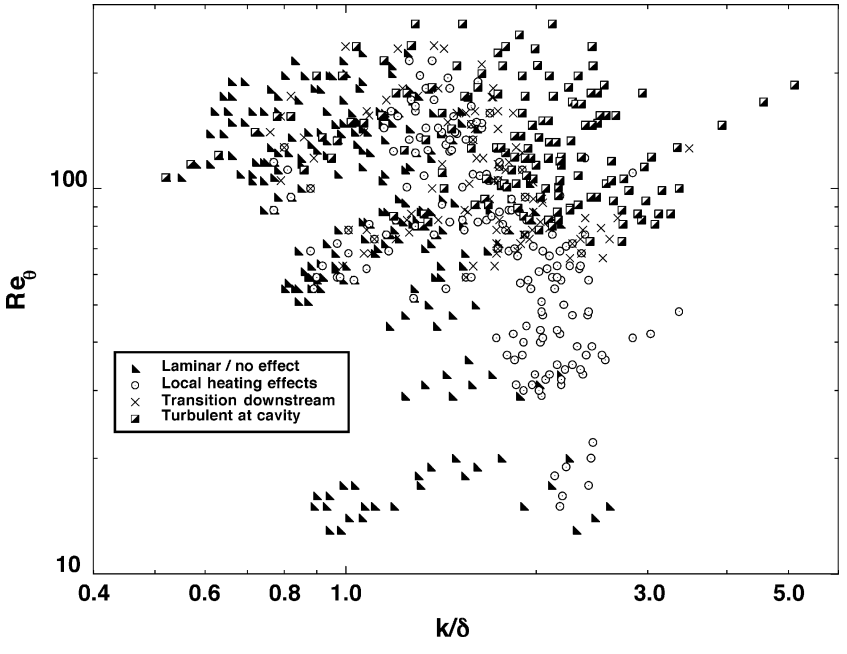

Fig. 17 Cavity effects as a function of Re_θ and k/δ.

of a cavity for a data point classified as "transition downstream." Additionally, because of the three-dimensional nature of the flow over this geometry at angle of attack, transitional/turbulent heating levels downstream of a cavity are highly dependent on the location of that cavity.

Correlation Parameters

Boundary-layer transition correlations are typically formulated in terms of the physical parameters of the tripping mechanism (e.g., steps, gaps, protuberances) and the fluid dynamic parameters of the boundary layer. Tripping parameters of interest are usually the diameter w, height or depth k, and location of the trip. Boundary-layer parameters of interest (obtained in this study from LAURA laminar flowfield computations) are usually the edge Mach number M_e, boundary-layer thickness δ, momentum thickness θ, boundary-layer-edge-temperature to wall-temperature ratio T_e/T_w, and edge Reynolds number based on momentum thickness and local flowfield quantities Re_θ. The data were analyzed to determine which of these parameters would be removed from consideration as correlation parameters and which were appropriate for use as correlation parameters.

In the current study, the test conditions were such that the shape factor δ/θ and the temperature ratio T_e/T_w deviated by less than 5% from average values of 7.35 and 1.6, respectively. Thus, θ and T_e/T_w could be eliminated as independent correlation parameters (although they might be factors at flight conditions).

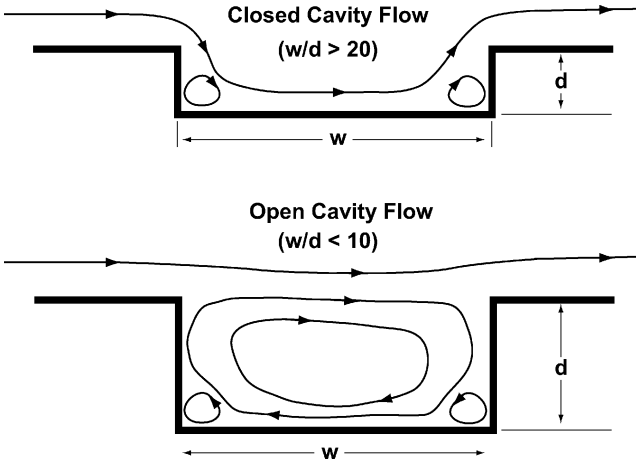

Fig. 18 Illustration of open- and closed-cavity flow types.

The data also showed that inclusion of the edge Mach number as a correlation parameter (in terms of Re_θ/M_e) made the correlations worse (that is, laminar, local, transitional, and turbulent data tended to overlap more when M_e was taken into consideration) than when only Re_θ was used. This result is in contrast to most correlations for discrete trips or protuberances, where Re_θ/M_e is typically one of the correlation parameters. However, it would seem appropriate for the current study because the boundary-layer disturbances were caused by cavities at the surface, not trips which extended toward the boundary-layer edge.

Finally, it was determined that cavity diameter w not cavity depth k was the appropriate length scale to use in correlating the data, as can be seen by comparing the groupings of data types in Figs. 16 and 17. The physical rationale for this behavior is that cavity parameters in the current data set indicate that open-cavity flows, as opposed to closed-cavity flows (e.g., Charwat et al.[22]), were produced in the test. Open-cavity flows skip over the cavity, whereas closed-cavity flows drop down into the cavity (Fig. 18) and are clearly influenced by the cavity depth. The boundary between open and closed flows occurs somewhere between cavity aspect rations w/d of 10 to 20, and in this study less than 5% of the data were obtained from cavities with w/d greater than 5.

Correlation Curve Fits

Based on the preceding analyses, the best correlation parameters were determined to be momentum Reynolds number Re_θ and the cavity-to-boundary-layer-height ratio w/δ. Examples of Re_θ and δ distributions over the vehicle are shown in Figs. 19–21. Curve fits were then generated to define boundaries between laminar and turbulent cavity effects. To identify which points would be used to generate the curve fits, the data were examined to determine at which values of Re_∞ fully turbulent flow at the cavity was first noted for fixed values of the cavity diameter w and location r/R and the model angle of attack α and orientation ϕ. These selected boundary points were curve fitted to generate the equation

$$Re_{\theta,\text{turb}} = 652.69 \times (w/\delta)^{-0.9214} \tag{1}$$

to define a lower bound for turbulence at a cavity. Similarly, the data points at the highest values of Re_δ at which laminar flow were last noted (for fixed values of w, r/R, α, and ϕ) were curve fitted to generate the equation

$$Re_{\theta,\text{lam}} = 2382.7 \times (w/\delta)^{-2.348} \tag{2}$$

to define an upper bound for laminar flow after a cavity. These curve fits and the data points used to generate them are shown in Fig. 22.

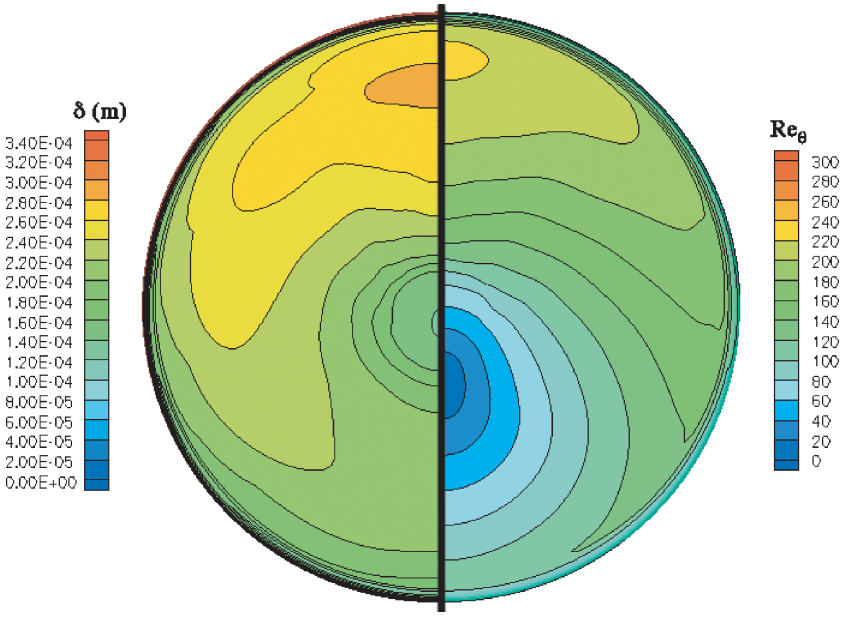

Fig. 19 Re_θ and δ distributions for $Re_\infty = 2.4 \times 10^7$/m and $\alpha = 11$ deg.

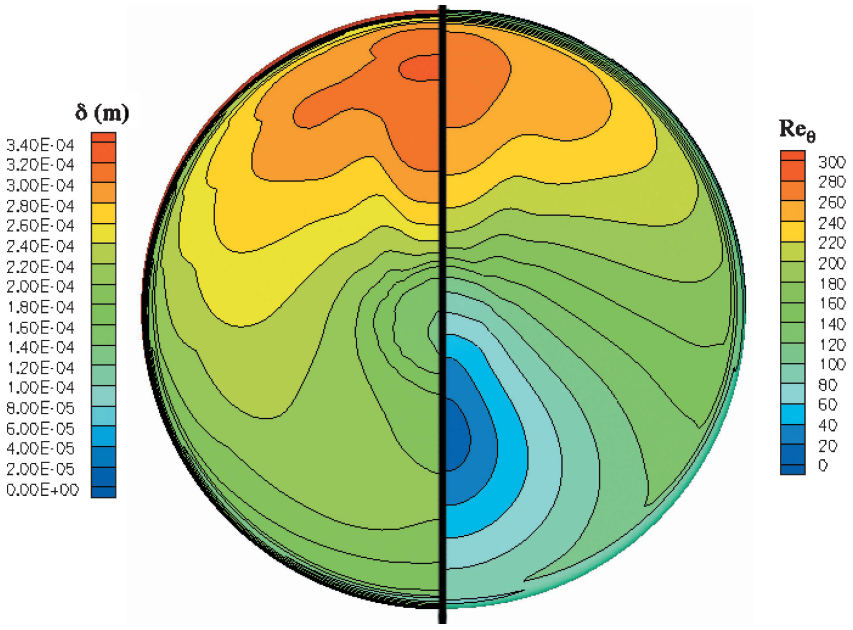

Fig. 20 Re_θ and δ distributions for $Re_\infty = 2.4 \times 10^7$/m and $\alpha = 16$ deg.

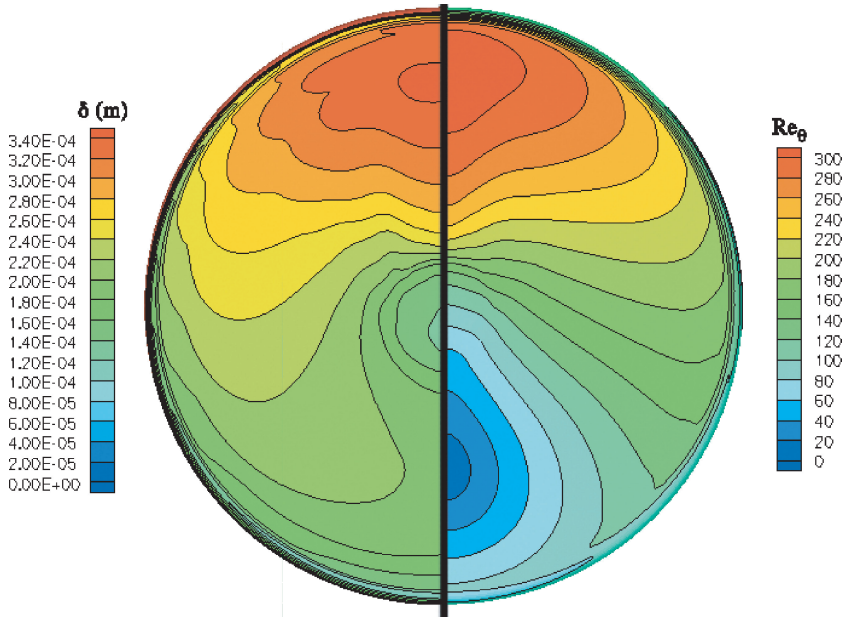

Fig. 21 Re_θ and δ distributions for $Re_\infty = 2.4 \times 10^7$/m and $\alpha = 20$ deg.

Almost all of the turbulent boundary points fell within the ±20% bands, but the laminar boundary points showed more scatter. Based on the range of test data, these fits should be applicable for Re_θ values of approximately 10–300 and w/δ values of 2–20.

These correlations are shown with the entire data set in Fig. 23. Although there is some scatter, the majority of the laminar and fully turbulent at cavity data points fall below or above the respective curves, while the local disturbance and transition downstream data points fall between the two curves. For design purposes, the lower, laminar boundary can be taken as the limit below which a cavity has no significant effect on heating or boundary-layer transition.

Critical Reynolds Number

If the exponent in the turbulent boundary point curve fit at −1, a critical Reynolds number

$$(Re_{w,e})_{\text{crit}} = \rho_e U_e w/\mu_e = Re_\theta (w/\theta) \tag{3}$$

as was first defined by Schiller[23] and employed by many other authors (e.g., Refs. 24–27), can be used to define a transition criteria. The new turbulent boundary fit becomes

$$Re_{\theta,\text{turb}} = 777.36 \times (w/\delta)^{-1} \tag{4}$$

This slightly different form of the turbulent boundary equation appears to fit the data as well as the form of Eq. (1), where the exponent was allowed to vary when determining the fit. Equation (4) can then be manipulated to yield

$$(Re_{w,e})_{\text{crit}} = 775.36(\delta/w)(w/\theta) = 775.36(\delta/\theta) = 5699 \tag{5}$$

with the constant value of 7.35 for the shape factor for these test conditions. This constant critical Reynolds number can be substituted into Eq. (3) to map a turbulent boundary over a vehicle for a specified cavity size. A sample mapping is shown in Fig. 24.

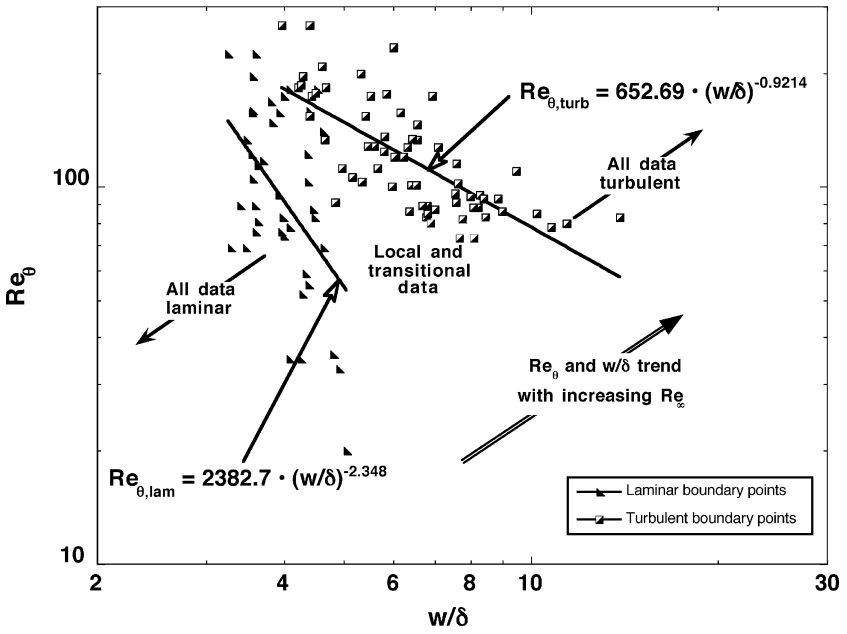

Fig. 22 Curve fits to wind-tunnel data points on the boundaries of laminar and turbulent flow.

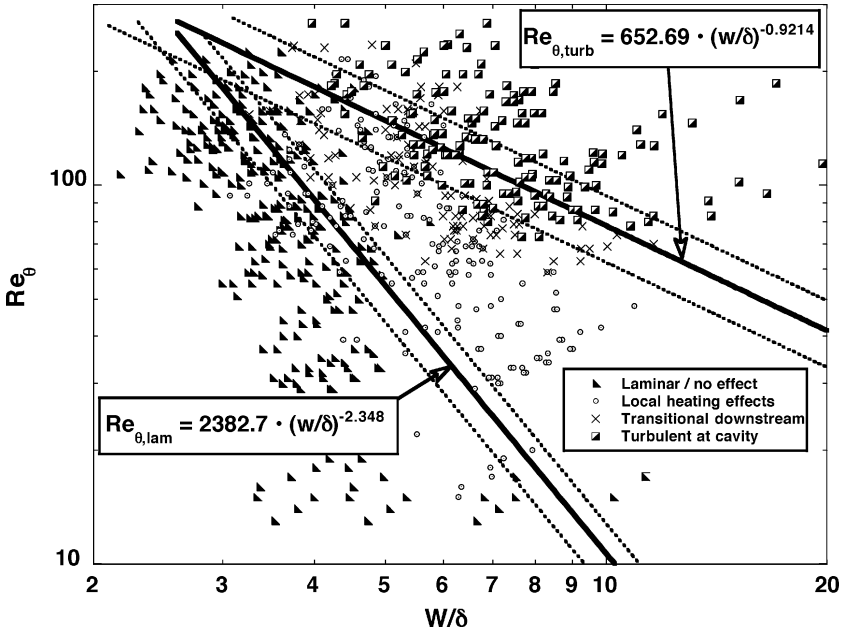

Fig. 23 Entire transition data set and correlations for laminar and turbulent boundaries.

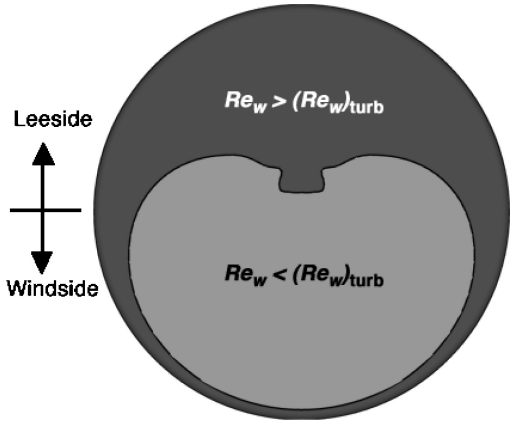

Fig. 24 Critical Reynolds-number boundary for $\alpha = 16$, $Re_\infty = 9.8 \times 10^6$/m, and largest cavity size.

Application to Flight Conditions

To determine whether cavities would have significant effects in flight, Re_θ and w/δ distributions were extracted from the flight computations presented by Edquist et al.[4] Typical centerline heating and momentum Reynolds-number distributions along the centerline are shown in Fig. 25 for the peak laminar heating point on the trajectory. It can be seen that the lee side of the vehicle experiences the highest Re_θ values when at angle of attack. Lee-side Re_θ and w/δ values for several trajectory points are plotted (on a linear scale in this figure) against the correlation curve fits in Fig. 26. Although these correlations were generated from data obtained in a perfect-gas air facility and might not be strictly applicable to nonequilibrium, Martian atmosphere conditions, they suggest that transition can be caused by the cavities well before the peak heating point on the trajectory, which would lead to higher heating rates and greater integrated heating loads downstream of the cavity. Because of this likelihood of early transition onset, as well as uncertainties in the prediction of the turbulent heating

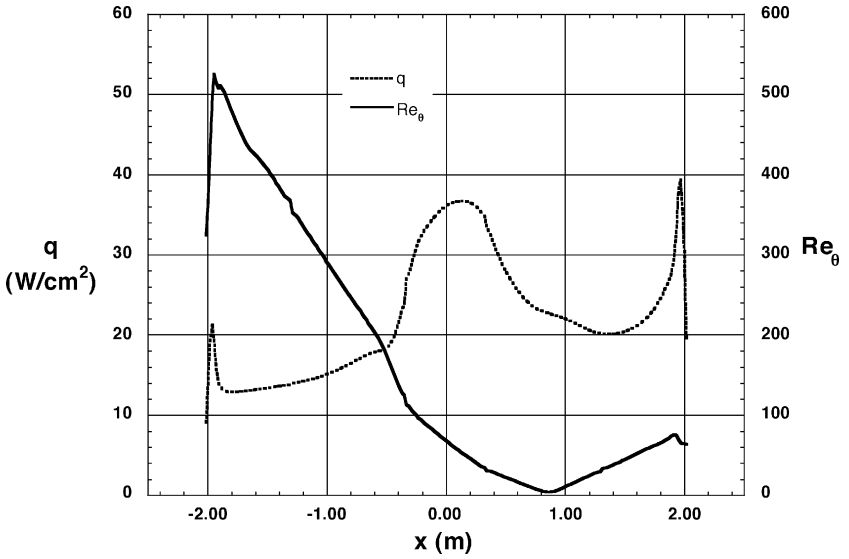

Fig. 25 Centerline heating and Re_∞ distributions for peak heating point on 2007 trajectory.

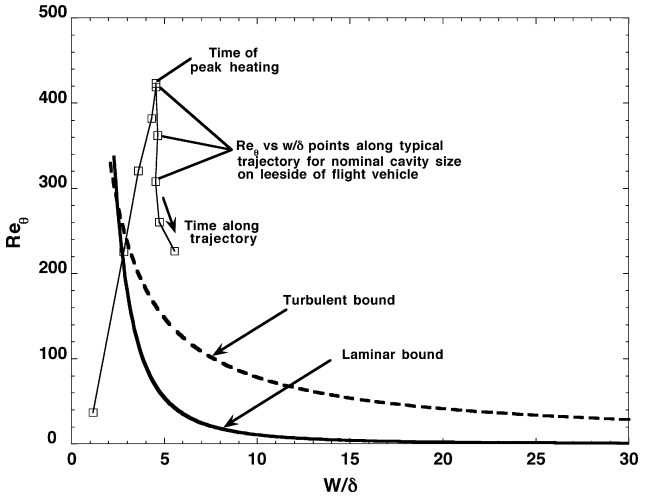

Fig. 26 Re_θ and δ values along 2007 trajectory compared to boundary-layer transition date and correlations.

levels resulting from cavity-induced transition, the forebody cavities were eliminated from the current MSL design by relocating the attachment points to the aftbody of the vehicle.

Summary

A computational and experimental study has been performed for the Mars Smart Lander to develop correlations for the effects of heat-shield cavities on the state of the boundary layer and to compare predicted and measured wind-tunnel heating levels.

Laminar Navier–Stokes predictions were found to agree with the laminar wind-tunnel data to within the estimated experimental uncertainty of the data. However, the agreement between turbulent Navier–Stokes predictions and experimental data was dependent on the location of transition specified in the computation and the diameter and location of the cavity on the test model. In general, zero-transition-length and natural-transition-length turbulent predictions bounded the shape of the experimental heating distributions, but for the larger cavities the measured heating levels exceeded the predictions by more than 20%. These differences were attributed to the use of a simple algebraic turbulence model in the computations and the exclusion of the actual cavity (and hence its effects on the flowfield) from the computational geometry.

Based on the turbulent experimental heating data, worst-case heating levels of up to 25% greater than at the nose were produced downstream of the largest cavity size located at the inner radial location. In contrast, although transition at the outer radial location occurred at lower freestream Reynolds numbers than for the inner location, there was insufficient running length downstream of the cavity for fully turbulent flow to develop, and so heating levels were lower. Thus, for aeroheating design considerations an outer radial location for a cavity would be preferable.

Boundary-layer-edge quantities were extracted from the laminar Navier–Stokes solutions and were used to correlate the experimental data on the state of the boundary layer. The correlations were expressed in terms of Re_θ and w/δ and can be used to determine whether a heat-shield cavity will have no effect on the boundary layer, will have a local effect, will produce transition downstream of the cavity, or will cause immediate transition to turbulent flow. A critical Reynolds number, which can be used to generate a surface transition map for given cavity size, was also defined. Application of these correlations to boundary-layer quantities determined from computations along the flight trajectory indicated that cavities would likely produce transition on the lee side of the heat shield well before the peak heating point on the trajectory. As a result, the cavities have been removed from the current MSL design by relocating the attachment points to the aftbody.

Acknowledgments

The authors thank the following persons at NASA Langley Research Center for their contributions to this work: Karl Edquist and Peter Gnoffo for assistance with the LAURA code; Steve Alter for generation of the computational grid; and Scott Berry for discussions on boundary-layer transition.

References

[1]Lockwood, M. K., Powell, R. W., Graves, C. A., and Carman, G. L., "Entry System Design Considerations for Mars Landers," American Astronautical Society, Paper AAS 01-023, Jan.–Feb. 2001.

[2]Lockwood, M. K., Powell, R. W., Sutton, K., Prabhu, R. K., Graves, C. A., Epp, C. D., and Carman, G. L., "Entry Configurations and Performance Comparisons for the Mars Smart Lander," *Journal of Spacecraft and Rockets*, Vol. 43, No. 2, 2006, pp. 258–269.

[3]Liechty, D. S., Hollis, B. R., and Edquist, K. T., "Mars Science Laboratory Experimental Aerothermodynamics with Effects of Cavities and Control Surfaces," *Journal of Spacecraft and Rockets*, Vol. 43, No. 2, 2006, pp. 340–353.

[4]Edquist, K. T., Liechty, D. S., Hollis, B. R., Alter, S. J., and Loomis, M. P., "Aeroheating Environments for a Mars Smart Lander," *Journal of Spacecraft and Rockets*, Vol. 43, No. 2, 2006, pp. 330–339.

[5]Cheatwood, F. M., Merski, N. M., Riley, C. J., and Mitchletree, R. A., "Aerothermodynamic Environment Definition for the Genesis Sample Return Capsule," AIAA Paper 2001-2889, June 2001.

[6]Gnoffo, P. A., "An Upwind-Biased, Point-Implicit Algorithm for Viscous, Compressible Perfect-Gas Flows," NASA TP-2953, Feb. 1990.

[7]Cheatwood, F. M., and Gnoffo, P. A., "User's Manual for the Langley Aerothermodynamic Upwind Relaxation Algorithm (LAURA)," NASA TM 4674, April 1996.

[8]Roe, P. L., "Approximate Riemann Solvers, Parameter Vectors and Difference Schemes," *Journal of Computational Physics*, Vol. 43, No. 2, 1981, pp. 357–372.

[9]Harten, A., "High Resolution Schemes for Hyperbolic Conservation Laws," *Journal of Computational Physics*, Vol. 49, No. 3, 1983, pp. 357–393.

[10]Yee, H. C., "On Symmetric and Upwind TVD Schemes," NASA TM 86842, Sept. 1985.

[11]Baldwin, B. S., and Lomax, H., "Thin Layer Approximation and Algebraic Model for Separated Turbulent Flow," AIAA Paper 78-257, Jan. 1978.

[12]Cheatwood, F. M., and Thompson, R. A., "The Addition of Algebraic Turbulence Modeling to Program LAURA," NASA TM-107758, April 1993.

[13]Dhawan, S., and Narashima, R., "Some Properties of Boundary Layer Flow from Laminar to Turbulent Motion," *Journal of Fluid Mechanics*, Vol. 1, Pt. 4, Jan. 1958, pp. 418–436.

[14]Fay, J. A., and Riddell, F. R., "Theory of Stagnation Point Heat Transfer in Dissociated Air," *Journal of Aeronautical Sciences*, Vol. 25, No. 2, 1958, pp. 73–85,

[15]Micol, J. R., "Hypersonic Aerodynamic/Aerothermodynamic Testing Capabilities at Langley Research Center: Aerothermodynamic Facilities Complex," AIAA Paper 95-2107, June 1995.

[16]Micol, J. R., "Langley Aerothermodynamic Facilities Complex: Enhancements and Testing Capabilities," AIAA Paper 98-0147, Jan. 1998.

[17]Hollis, B. R., "Real-Gas Flow Properties for NASA Langley Research Center Aerothermodynamic Facilities Complex Wind Tunnels," NASA CR 4755, Sept. 1996.

[18]Buck, G. M., "Automated Thermal Mapping Techniques Using Chromatic Image Analysis," NASA TM 101554, April 1989.

[19]Buck, G. M., "Surface Temperature/Heat Transfer Measurement Using a Quantitative Phosphor Thermography System," AIAA Paper 91-0064, Jan. 1991.

[20]Merski, N. R., "A Relative-Intensity, Two-Color Phosphor Thermography System," NASA TM 104123, Sept. 1991.

[21]Merski, N. R., "Global Aeroheating Wind-Tunnel Measurements Using Improved Two-Color Phosphor Thermography Methods," *Journal of Spacecraft and Rockets*, Vol. 36, No. 2, 1999, pp. 160–170.

[22]Charwat, A. F., Roos, J. N., Dewey, C. F., and Hitz, J. A., "An Investigation of Separated Flows—Part I: The Pressure Field," *Journal of the Aerospace Sciences*, Vol. 28, No. 6, 1961, pp. 457–470.

[23]Schiller, L., "Flow in Pipes," *Handbook of Experimental Physics*, Vol. 4, Pt. 4, Academic Press, Leipzig, Germany, 1932, pp. 189–192.

[24]Reda, D. C., "Correlation of Nosetip Boundary-Layer Transition Data Measured in Ballistic Range Experiments," *AIAA Journal*, Vol. 19, No. 3, 1981, pp. 329–339.

[25]Poll, D. I. A., "The Effect of Isolated Roughness Elements on Transition in Attachment-Line Flows," *Laminar-Turbulent Transition*, edited by D. Arnal and R. Michel, Springer-Verlag, New York, 1990, pp. 657–667.

[26]Bouslog, S. A., Bertin, J. J., Berry, S. A., and Caram, J. M., "Isolated Roughness Induced Boundary-Layer Transition: Shuttle Orbiter Ground Tests and Experience," AIAA Paper 97-0274, Jan. 1997.

[27]Berry, S. A., Bouslog, S. A., Brauckmann, G. J., and Caram, J. M., "Shuttle Orbiter Experimental Boundary-Layer Transition Results with Isolated Roughness," *Journal of Spacecraft and Rockets*, Vol. 35, No. 3, 1998, pp. 241–248.

M. K. Lockwood
Guest Editor

Color reproductions courtesy of NASA Langley Research Center.